Tracking transient changes in the plumbing system at Campi Flegrei Caldera

G. Giacomuzzi [a,*], C. Chiarabba [a], F. Bianco [a], P. De Gori [a], N. Piana Agostinetti [b]

[a] National Institute of Geophysics and Volcanology, Via di Vigna Murata 605, 00143 Rome, Italy
[b] Department of Earth and Environmental Sciences, Milano Bicocca University, Piazza della Scienza 1, 20126 Milan, Italy

ARTICLE INFO

ABSTRACT

Increase in seismicity, gas emission and ground uplift are symptoms of unrest in Quaternary calderas. Since the raising of the alert level in 2012, their continuous increase in the Campi Flegrei caldera is generating growing concerns for such a densely populated area. Until now, we never detected the injection of fresh magma in the shallow system, leaving uncertainties on the proximity of an eruption. Here, we show evidence for episodic refills of magma and magmatic fluids in shallow and deep reservoirs beneath the resurging area, revealed by a new fully non-linear 4D (in space and time) seismic tomography. Transient signatures in tomograms depict the ascent of magma batches at shallow depth, which could have started in 2019, perturbing the shallow circulation of hydrothermal fluids. The existence of a similar signature also during the 1982–84 episode, suggests that accumulation of magma batches may be a common way of caldera to grow. Anyway, the ability to fast track changes associated with magma ascent is crucial to forecasting and modeling how restless calderas evolve and may become prone to erupt.

1. Introduction

Unrest episodes generally herald volcanic eruptions, but not always in many calderas (Newhall and Dzurisin, 1988; Acocella et al., 2015). Although eruptions can occur also without clear warning, the possibility to capture precursory feeble signals is the main challenging purpose of volcanic monitoring (Rosi et al., 2022). The Campi Flegrei is one of the most famous Quaternary calderas of the world, where the term ''bradyseism'' originated to describe the cyclic ground uplift and subsidence observed through time. Besides the two gigantic eruptive events at 40 ka (the Campanian Ignimbrite eruption) and at 15 ka ago (the Napolitan Yellow tuff), that caused the collapse and formation of the caldera, at least 70 smaller eruptions are documented in more recent times (Di Vito et al., 1999; Orsi et al., 2004; Pappalardo and Mastrolorenzo, 2012). In the last one (1536 ad), the magma erupted after a period of long-term precursory phenomena (Di Vito et al., 2016; Trasatti et al., 2023), possibly indicating the beginning of a new caldera cycle (Forni et al., 2018).

Since 2005, variation in the gas composition within the caldera fumaroles (Chiodini et al., 2016; 2021), ground uplift (De Martino et al., 2021) and seismic energy release (Tramelli et al., 2022; Danesi et al., 2024) resumed, leading to hypothesize that an intrusion of magma interrupted the long period of dominant hydrothermal activity (D'Auria et al., 2015). The present-day escalation in seismicity (Fig. 1b) and surface gas emissions has been interpreted as due to a pressure-temperature increase at the top of a vertically elongated gas front (Chiodini et al., 2021; Giudicepietro et al., 2021; Akande et al., 2021).

A consensus exists on the existence of a central shallow intrusion at about 3.5 km depth, responsible for historical activity and unrest (Amoruso et al., 2014; Rosi et al., 2022; Acocella, 2019; Amoruso and Crescentini, 2022; Di Vito et al., 2016; De Siena et al., 2017a). The nature of the intrusion is a matter of debate, because the presence of magma at shallow depth (< 7 km) has been never revealed so far. Seismic reflection investigations point to the existence of a magmatic storage zone at 7 km depth (Zollo et al., 2008). Petrological data also suggest the existence of a multi-depth magmatic system (Buono et al., 2022; Pappalardo and Buono, 2021), constituted by a shallow (150–200 MPa, corresponding to 6–8 km) reservoir recharged by a deeper one (400 MPa, about 16 km).

Several pieces of evidence indicate that the central sill is covered by a "caprock" formation which, thanks to its particular mechanical

---

properties, acts as a barrier for the propagation of the upwelling magmatic materials to the surface (Vanorio and Kanitpanyacharoen, 2015; De Siena et al., 2017b; Calò and Tramelli, 2018; Akande et al., 2019, 2021; Lima et al., 2021) . The caprock would allow the system to accommodate larger strain, as fluids accumulate and pore fluid pressure builds up in the gas-bearing overpressured formations lying underneath, and to regulate fluids interchange between the deep source and the shallow hydrothermal system. Alternation over time of self-sealing processes and degradation of the mechanical properties of the caprock may be responsible for the caldera unrests, without the need of a magmatic intrusion (Lima et al., 2021).

Whether the ongoing unrest is directly related to fresh magma injection or to the stimulation of the hydrothermal system by fluid expulsions from a deeper magmatic source is the main question today (D'Auria et al., 2015; Moretti et al., 2020; Lima et al., 2021; Buono et al., 2022). Despite the huge number of published multidisciplinary investigations and debates on the recent unrest episode, some crucial questions are still without answers and consensus in the scientific community: What is the depth of the magma reservoirs infilled in the last decades? And, most important, is there an active magma inflation in the actual unrest? Up to now, local earthquake tomography (LET) proved to be an effective tool to image the Vp and Vp/Vs structure beneath the Campi Flegrei caldera, but with a resolved volume limited to the upper 4 km depth. (Vanorio et al., 2005; Chiarabba and Moretti, 2006; Battaglia et al., 2008; De Siena et al., 2010; Priolo et al., 2012; Calò and Tramelli, 2018). Here, we show that if the LET problem is solved by a fully non-linear and trans-dimensional Bayesian approach (Giacomuzzi, 2013; Piana Agostinetti et al., 2015, 2017), with a self-adaptive parametrization of the earth volume, the structure of the magmatic system can be enlightened also at greater depth. Moreover, this novel method enables the detection of first order transient variations of seismic velocities over time.

2. Data and method

2.1. Seismic data and network

The seismic dataset consists of 16669 P- and 8292 S-waves arrival-time measurements of 1894 local earthquakes, recorded between January 1984 and December 2022. The 1984 dataset has been already used in previous tomographic investigations (Vanorio et al., 2005; Chiarabba and Moretti, 2006) and consists of 2289 P-wave and 1691 S-wave arrivals of 338 micro-earthquakes, recorded at 21 three-component digital stations (Fig. 1a). Earthquakes were selected based on azimuthal gap (<180°), 1d-location errors (<1 km) and minimum number of phases (7 P-phases and 3 S-phases). The same criteria were used in the selection of arrival time data for the 2005–2022 period. We obtained a total of 14,380 P-phases and 6601 S-phases of 1556 micro-earthquakes, recorded by 43 stations. The array distribution was different in 1984 compared to later periods, while it can be considered unchanged after 2016.

For the computation of the 3D model, we also included 15,041 P-wave arrivals from 409 shots (2001 SERAPIS project, Zollo et al. 2003, 2008). The seismic active data allow illuminating the upper 1–2 km of the crust in the offshore part of the caldera, with most of the rays crossing at 1 km depth. Further details about the active data acquisition can be found in Zollo et al. (2003).

Real uncertainties on phase pickings are generally poorly known, as data were gathered by different operators in different periods. The noise level is therefore treated as an unknown parameter (Bodin et al., 2009), overcoming the problem of possible inconsistency in the errors estimation between different dataset and operators. The noise level includes noise in seismic waveforms, differences in picking of arrival times by different operators and inaccuracies due to approximations in forward modeling. We considered two different noise levels for P-wave and S-wave data, which rescale picking uncertainties ($\varepsilon_s = 10^{(n+Log(\varepsilon_p))}$; $\varepsilon_s =$
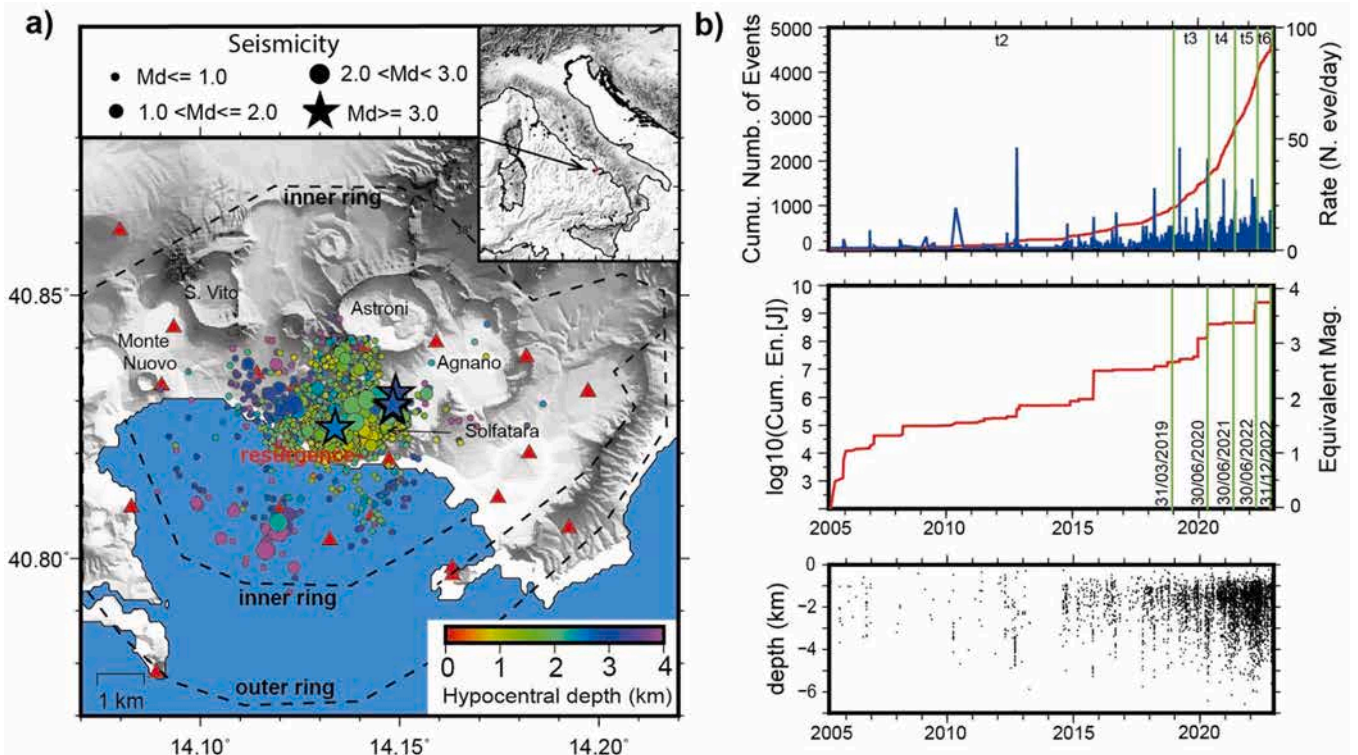

Fig. 1. Map of Campi Flegrei caldera and seismicity distribution. a) Map of the investigated area showing the seismic stations network (red triangles) and seismicity. Inner and other rings redrawn from Natale et al. (2022). b) Evolution of seismicity since the beginning of the current unrest (2005). Green vertical lines mark time steps (t2-t6) considered in the 4D tomography. Upper panel: cumulative number of events (red) and seismic rate (blue). Central panel: cumulative energy release and equivalent magnitude. Lower panel: time evolution of hypocentral depths.

estimated picking uncertainties (s), n= unknown noise level, ε_p= starting picking uncertainties). Approximate starting picking uncertainties were derived from the SAC weighting scheme 0–3 (weight 0 = 0.02 s, weight 1 = 0.05 s, weight 2 = 0.1 s, weight 3 = 0.3 s).

2.2. 3D non-linear trans-dimensional local earthquake tomography

In this study, we used the trans-D LET code developed by Piana Agostinetti et al. (2015) to compute an enhanced Vp and Vp/Vs 3D static model below the caldera. In this section, we briefly described the method; more details and mathematical formulation can be found in Giacomuzzi (2013) and Piana Agostinetti et al. (2015). The main advantages of this novel method, with respect to more diffused linearized approaches, are (i) the independence of the solution from the starting models (which choice is always somewhat arbitrary), (ii) the fact that the solution is not just a best-fit model, but a set of (thousands) models that fit the observed data in a similar way and (iii) the use of a self-adaptive parameterization, which allows not having to impose any type of regularization to solve the non-uniqueness of the inverse problem solution.

In the Bayesian approach, the solution of the LET problem (i.e., the joint estimation of P-wave velocity (Vp), Vp/Vs ratio, and hypocentral locations from P- and S-waves arrival times) is a posterior probability density distribution (PPD), which fully describes the probability of a model to be the real one, given the observed data. It can be derived from Bayes's theorem, by combining the likelihood function with the a-priori density function. The likelihood function describes the probability of getting the observed data given a particular model, while the a-priori density function describes our a-priori knowledge about model parameters. If the observed data provide no new information, the posterior coincides with the prior density function.

The investigated crustal volume (about 20 km x 20 km x 8 km) covers the entire caldera and it is parameterized by an ensemble of 3D Voronoi's cells (Fig. 2). The parametrization is self-adaptive (Bodin et al., 2009), because the number and position of the Voronoi's cells are considered as unknowns and directly estimated from data. Each ensemble of Voronoi's cells is rasterized on a Cartesian 3D regular grid of nodes (spacing is 0.5 km in x,y and z directions), whose Vp and Vp/Vs values are the values at the nearest Voronoi's nucleus. The grid defines the minimum spatial resolution of the model. The same Cartesian grid is used to solve the forward problem (i.e., the computation of theoretical travel times from source to receivers), with the Pseudo-bending ray-tracer (Um and Thurber, 1987), and to compute the posterior mean velocity model.

To build the PPD, we defined a-priori probability density distributions for all the unknown parameters (Table S1) and used the Reversible Jump Markov Chain Monte Carlo Method (Rj-McMc) to generate samples of the PPD (Green, 2003). Along each Markov chain, for each new candidate model drawn from the prior distribution, the algorithm computes the likelihood function (least square misfit). Then, the candidate model is accepted according to the Metropolis rule (Green, 2003). We run 20 independent Markov Chains, each of which starting from different initial models drawn from the prior distribution. Accepted models are considered samples of the PPD after all chains reached the convergence state (Fig. S1).

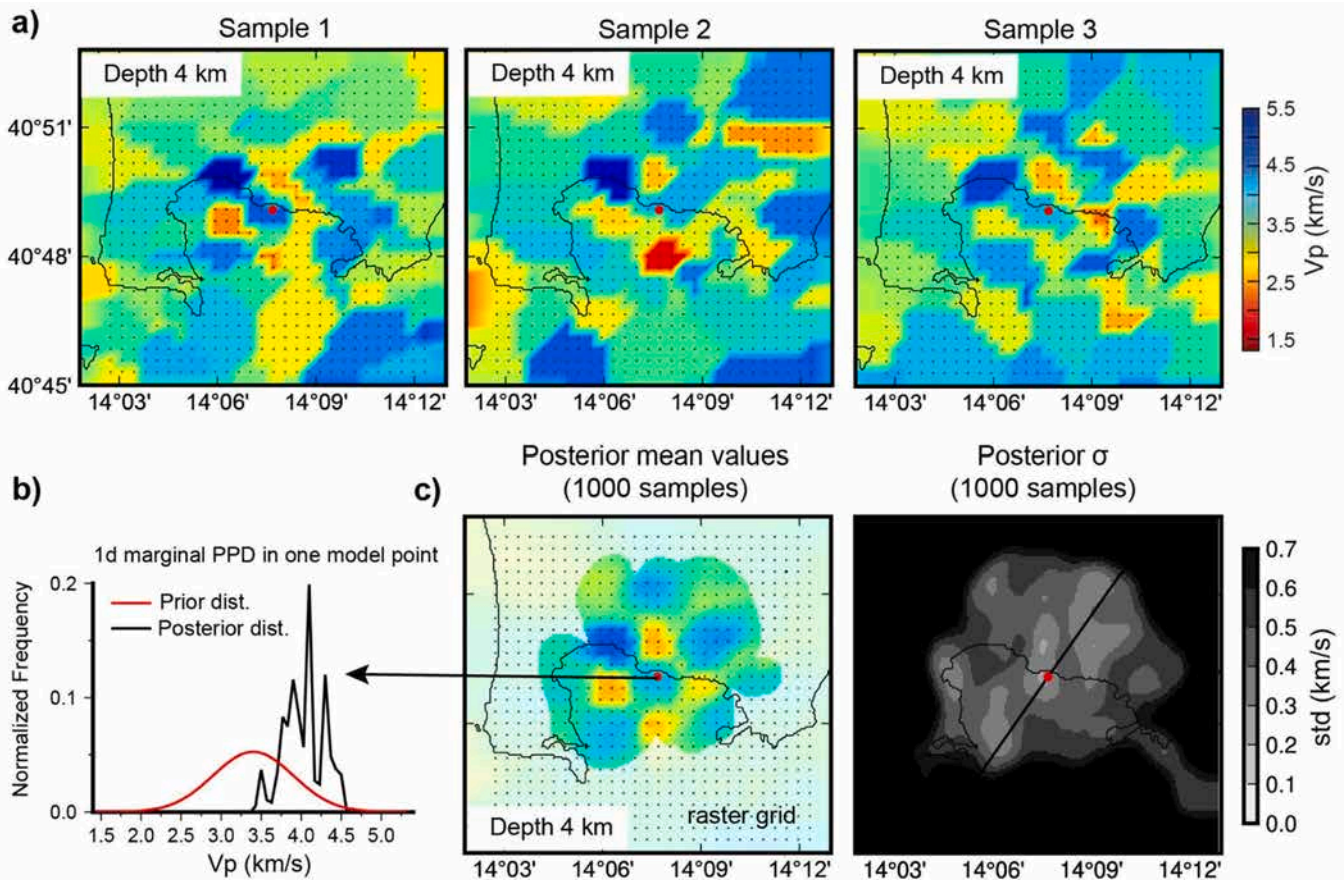The convergence is reached when the noise level of both P- and S-

Fig. 2. Model parameterization and computation of 1d-marginal PPD: a) example of three samples of the PPD collected along a Markov chain. The three different ensembles of Voroinoi's cell are rasterized on the Cartesian grid before plotting. b) Example of 1d marginal PPD (probability distribution over the Vp value in one point of the model) computed from 1000 PPD samples and compared with the prior distribution. 1d-marginal PPDs are computed for each of the grid nodes. c) Posterior mean and standard deviation values calculated from each of the 1d-marginal PPD.

waves oscillates around a constant value and the number of models accepted with a deteriorated fit is similar to the number of models accepted with an improved fit. Finally, statistical estimators, such as mean values of individual parameters and the associated standard deviations, are derived from the PPD, by constructing 1D marginal probability functions, i.e. the density function obtained by integrating out all but one parameter (Fig. 2b).

The overall root mean square residuals computed in the mean posterior 3D model are equal to 0.008 s (P-waves) and 0.018 s (S-waves). The values are 59 % and 84 % lower if compared to those calculated in the prior model (Fig. S2). The final P- and S-phases noise levels amount to 0.2 and 0.1, respectively, indicating an overall underestimation of picking uncertainties (e.g. the estimated P-phase picking uncertainty of a 0-weight phase is 0.03 s instead of 0.02 s, of a 2-weight phase is 0.15 s instead of 0.1 s).

2.3. From 3D to 4D tomography

In order to evaluate transient time changes in the velocity structure, we extended the method used for the 3D tomography, by adding an unknown time-coordinate to the Voronoi's cells parameters. From a mathematical point of view, there is no significant difference in the method between 3D and 4D tomography. The 4 space-time coordinates x,y,z,t are a-dimensional and are characterized by uniform prior distributions in the model domain. The main difference is in the forward computation, performed by cutting the 4D Vp and Vp/Vs model formed by the Voronoi's cells distribution at predefined calendar times (called time-steps hereinafter).

For each time-step, the 4D cells distribution is rasterized on a Cartesian 3D grid, by associating at each of the grid nodes the Vp and Vp/Vs of the nearest Voronoi's cell (nearest in both space and time). Travel times are then computed for each earthquake in the 3D grid closest to its origin time. The main difference, and improvement, from previous approaches to 4D tomography (the so called time-lapse tomography, Patanè et al. 2006; Chiarabba et al. 2009, 2020) is that consecutive 3D velocity models (at consecutive time-steps) will share the same 4D Voronoi's cells if the data do not support any change in velocity over time, strongly reducing the number of model parameters to be estimated. In fact, trans-dimensional algorithms are naturally "parsimonious" (Malinverno, 2000) and would not introduce features un-supported by data, both in space and time. In other words, transient changes in velocities are intrinsically discouraged if not really required by data. This approach mitigates possible artifacts or spurious time changes generated by an uneven volume sampling during different epochs.

The time-steps (Table S2) were chosen based on time evolution of seismicity and travel time residuals computed in the posterior mean 3D model (Fig. S2b). The first time-step includes the whole 1984 seismicity, the second one (2005–04/2019) was chosen large enough to include an acceptable number of deep earthquakes (> 4 km), able to illuminate the deep structure. At the end of this time interval (2018–2019), S-waves traveltime residuals are notably high and the seismicity shows a further deepening, suggesting a notable change in seismic velocities. The remaining time-steps were chosen based on the main steps observed in seismic rate and energy release (Fig. 1b). The prior distributions of Vp and Vp/Vs (Table S1) have the same standard deviations used in the 3D tomography (Vp =0.7 km/s, Vp/Vs =0.3) and mean values equal to the posterior mean values of the 3D model. This choice doesn't affect the results, being the prior standard deviations as high as in the 3D tomography, but permits to save a lot of time in looking for high probability regions of the PPD, and so speeding up the convergence of the chains.

The root mean square residuals calculated in the mean 4D model are equal to 0.004 s (P-waves) and 0.013 s (S-waves), achieving a further reduction of 17 % (P-waves) and 5 % (S-waves) if compared to the 3D tomography (Fig. S2). The final P- and S-phases noise levels resulting from the 4D tomography are 0.1 and 0.06, respectively.

2.4. Resolution assessment in non-linear tomography

Model resolution for both the 3D and 4D inversions has been investigated by comparing prior and posterior density distributions over velocity parameters, by means of synthetic tests, and by analyzing raypaths distributions. Bayesian approach goes beyond the analysis of the resolution matrix traditionally computed in linearized tomography (Sambridge, 1990; Mosegaard and Sambridge, 2002), where the solution of the damped least square inversion problem is a single best-fitting likelihood model. Our "solution" is not just a single model, but an ensemble of models distributed according to the PPD. At every point of the model, if the posterior σ of the 1d-PPD is lower than the prior one, some new information has been extracted from data and added to our prior knowledge about the model. It's noteworthy that, in the 3D tomography, a small reduction in σ may be due to both a poor ray-coverage and the occurrence of transient velocity changes. In the 4D tomography, it also occurs if predetermined time-steps are not close enough to detect transient changes in velocity parameters. Moreover, where a small σ reduction is associated with a posterior mean velocity value quite similar to the prior one, the reliability of the model in that point is of course questionable.

To fully assess model resolution, we performed several synthetic tests (Rawlinson and Spakman, 2016), provided as supplementary material (Figs. S3-S16). Synthetic tests were done by mirroring, as much as possible, the real data inversion (similar prior distributions, similar recipe of sampling the parameter space, same number of models generated along Markov Chains, same data noise). Synthetic noise was generated with a Gaussian distribution consistent with that obtained a-posteriori from the real data, i.e. by including the P- and S- noise levels obtained in the real data tomography. The Vp and Vp/Vs prior models are the same for 3D and 4D synthetic tests (1D Vp model, σ=0.7 km/s and uniform Vp/Vs=1.8 model, σ=0.3).

We performed three kinds of tests for both the 3D and 4D tomography: (i) the checkerboard test, with the purpose to obtain a global view of model resolution (Figs. S3-S7), (ii) two spike tests, testing the main anomalies observed in the real data tomography (Figs. S8-S9,S11-S15) and (iii) further tests aiming to simulate the existence of a caprock thin layer at 2 km depth in the 3D model (Fig. S10) and of coarser structures in the 4D model (Fig. S16). Hypocentral parameters were also estimated in the synthetic tests. In this section, we describe the 3D and 4D checkerboard tests, while the other tests are described in the Results section.

The results of the 3D checkerboard test (Figs. S3-S4) show that the checkerboard structure is well recovered below the central part of the caldera in both the Vp and Vp/Vs models, down to 5–6 km. It is noteworthy that the checkerboard structure is recovered also where the ray-coverage is apparently scarce, although with an underestimation in amplitude and some smearing of anomalies along the ray-paths. Our novel method is able to extract more information from the observed data on poorly sampled model volumes if compared to linearized approaches (Giacomuzzi, 2013; Piana Agostinetti et al., 2017). Since both sources and receivers are usually unevenly distributed in space, the data information content is heterogeneous and the model is characterized by both well and ill-constrained volumes. With a fixed model parameterization, the existence of ill-constraint parameters is a source of non-uniqueness in the solution and the inversion usually requires some regularization, enhancing the difference in data resolution power between well and poorly sampled volumes. Usually, the regularization over-damps changes in poorly sampled volumes, further reducing the intrinsic data resolution power. The absence of regularization avoids the loss of data information and also reduces the smearing and damping of individual parameters toward the surrounding volume, allowing to recover both lateral and vertical sharp velocity changes. These are fundamental advantages of non-linear, self-regularizing tomography, that permits to

define and resolve larger volumes than classical linearized schemes, especially those where the illumination by seismic rays is apparently minor.

The 4D checkerboard test (Figs. S5-S7) was designed to evaluate smearing along the time axis and possible loss of resolution compared to the 3D case. The input checkerboard structure is present in the t1, t4-t6 time-steps and it is absent in the t2 and t3 time-steps. The changes over time in the checkerboard structure are generally well recovered, with smearing along the time axes of about 10 % of absolute velocities (i.e. for Vp=4 km/s, possible artifacts amounts to 0.4 km/s). The comparison
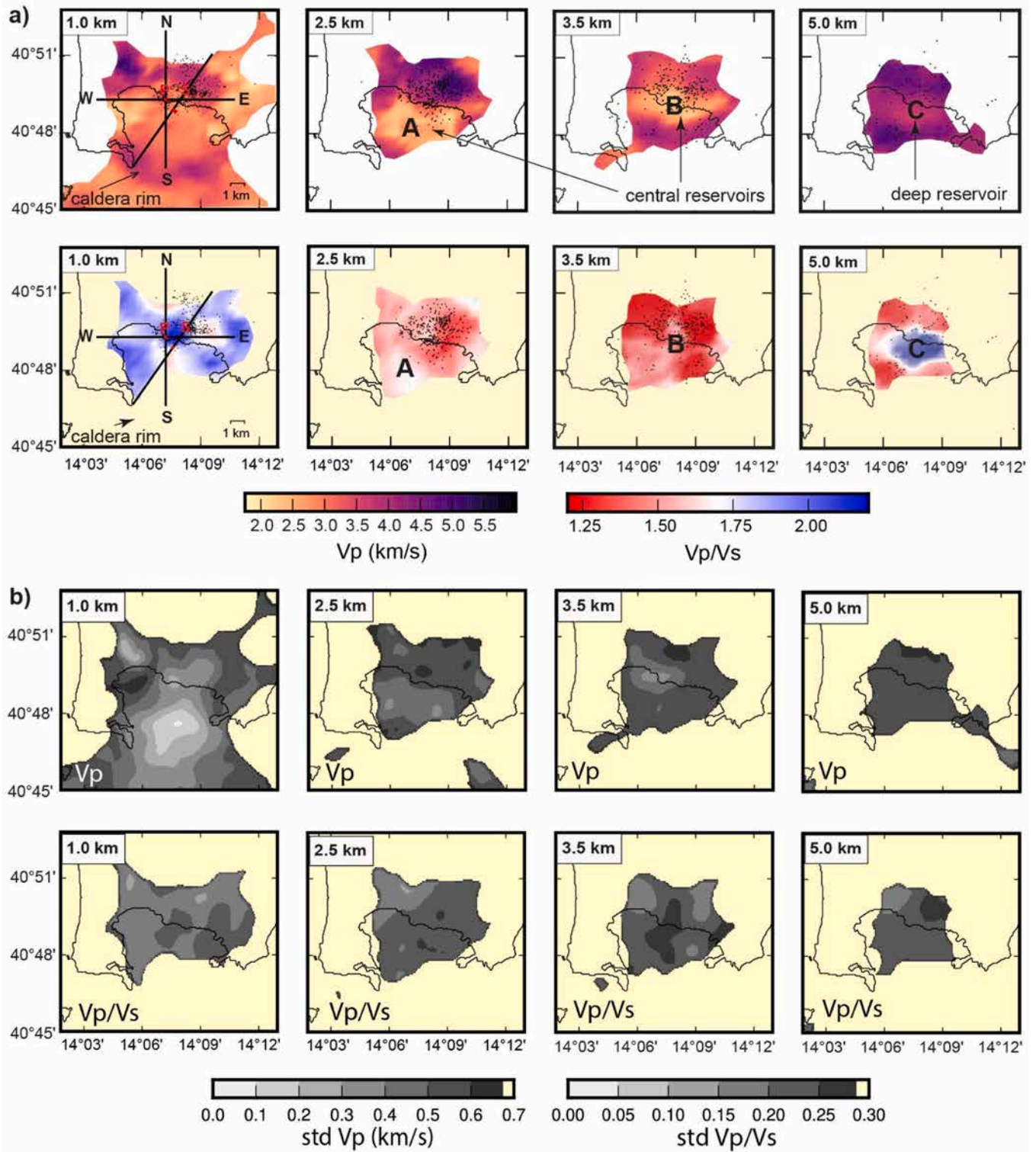

Fig. 3. 3D Vp and Vp/Vs posterior models. a) Mean posterior Vp (upper panels) and Vp/Vs (lower panels) values plotted on horizontal layers at 1, 2.5, 3.5 and 5 km depth. Uniform white and yellow areas indicate not-resolved model regions. Black dots: earthquakes distant less than 0.5 km from the layers. P: Pozzuoli town, S: Solfatara emission zone. A, B and C: main anomalies discussed in the text. b) Posterior Vp standard deviations (upper panels) and posterior Vp/Vs standard deviations (lower panels) plotted on the same layers.

between the 3D and 4D checkerboard tests shows that the retrieved anomalies are similarly resolved down to 4 km depth. A partial loss of resolution (decreased recovered amplitude and smearing) occurs at greater depth in the 4D tomography. Nevertheless, in the central part of the caldera, the resolution is good enough to detect the checkerboard anomalies to 4.5–5 km depth also in the 4D tomography.

3. Results

3.1. 3D Vp and Vp/Vs models

The 3D Vp and Vp/Vs models (Figs. 3 and 4) highlight the first-order structures of the plumbing system. A strong low Vp (down to 2.15 km/s)
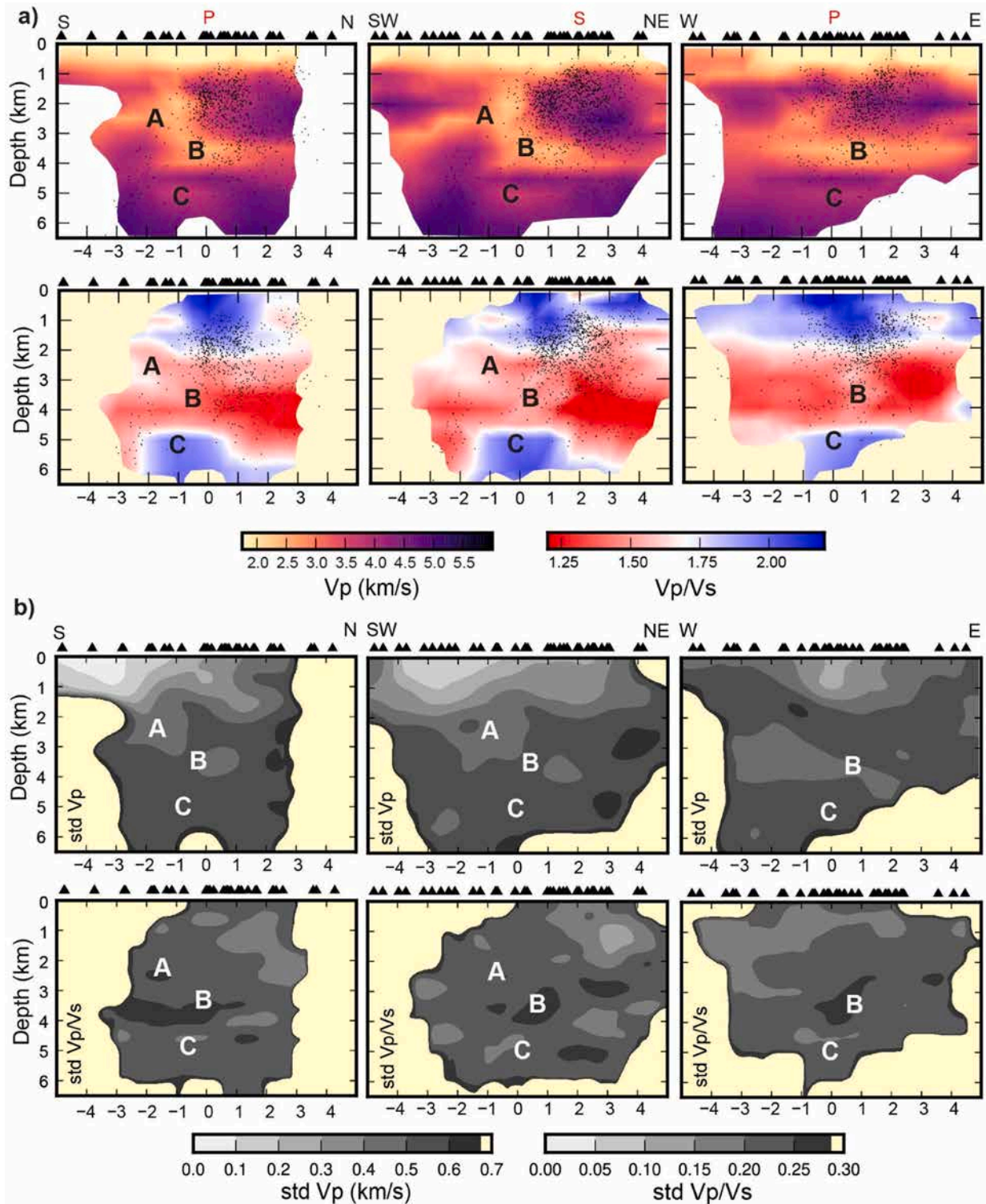

Fig. 4. 3D Vp and Vp/Vs posterior models. a) Mean posterior Vp (upper panels) and Vp/Vs (lower panels) values plotted on S-N, SW-NE and W-E vertical sections (locations in Fig. 3). Uniform white and yellow areas indicate not-resolved model regions. Black dots: earthquakes distant less than 1.5 km from the sections. P: Pozzuoli town, S: Solfatara emission zone. Triangles: stations distant less than 2 km from the section. A, B and C: main anomalies discussed in the text. b) Posterior Vp standard deviations (upper panels) and posterior Vp/Vs standard deviations (lower panels) plotted on the same sections.

and variable Vp/Vs (1.3–1.75) anomaly is observed beneath the center of the caldera, in between 2 and 4 km depth, surrounded by much higher Vp rocks (up to 5 km/s). The low Vp anomaly spreads towards S-SW at 2.5 km depth (anomaly A) and toward NE-E at 3.5–4 km depth (anomaly B). A second low Vp (3.2–4 km/s) and high Vp/Vs (1.9–2.1) anomaly is located at 5 km depth (anomaly C), separated by the overlying B anomaly by a high Vp layer. The posterior σ_{Vp} (Figs. 3b and 4b) in correspondence of these main anomalies vary from 0.2 to 0.5 km/s (0–3 km depth) to 0.5–0.6 km/s (3–6 km depth). The posterior $\sigma Vp/Vs$ amount to 0.2–0.25. Higher posterior $\sigma Vp/Vs$ values are observed locally in between 3 and 4 km depth. The overall high values of the posterior σ may be considered an indication of remarkable velocity changes over time, which cannot be fitted by the 3D model. Conversely,

the posterior σ reaches the lowest values (<0.2 km/s) to the south of the caldera, down to 2 km depth, i.e. in the volume mainly sampled from the Serapis project data, all collected in 2000.

Moreover, despite the high values of posterior σ, all the A, B and C anomalies can be considered reliable, because their Vp and Vp/Vs values differ significantly from the prior values (A anomaly: Vpprior=2.8 km/s, Vp/Vsprior=1.8, B anomaly: Vpprior=3–3.5 km/s, Vp/Vsprior=1.8, C anomaly: Vpprior=4.0 km/s, Vp/Vsprior=1.8).

To further test the reliability of the A, B and C anomalies, we performed two separate 3D spike-tests (Figs. S8-S9), with input anomalies of size 2 km x 2 km, in the horizontal directions, and 0.5–0.75 km in the vertical one, and amplitudes similar to those obtained in the real data tomography (A and B anomalies: Vp=2.15 km/s, Vp/Vs=1.5, C

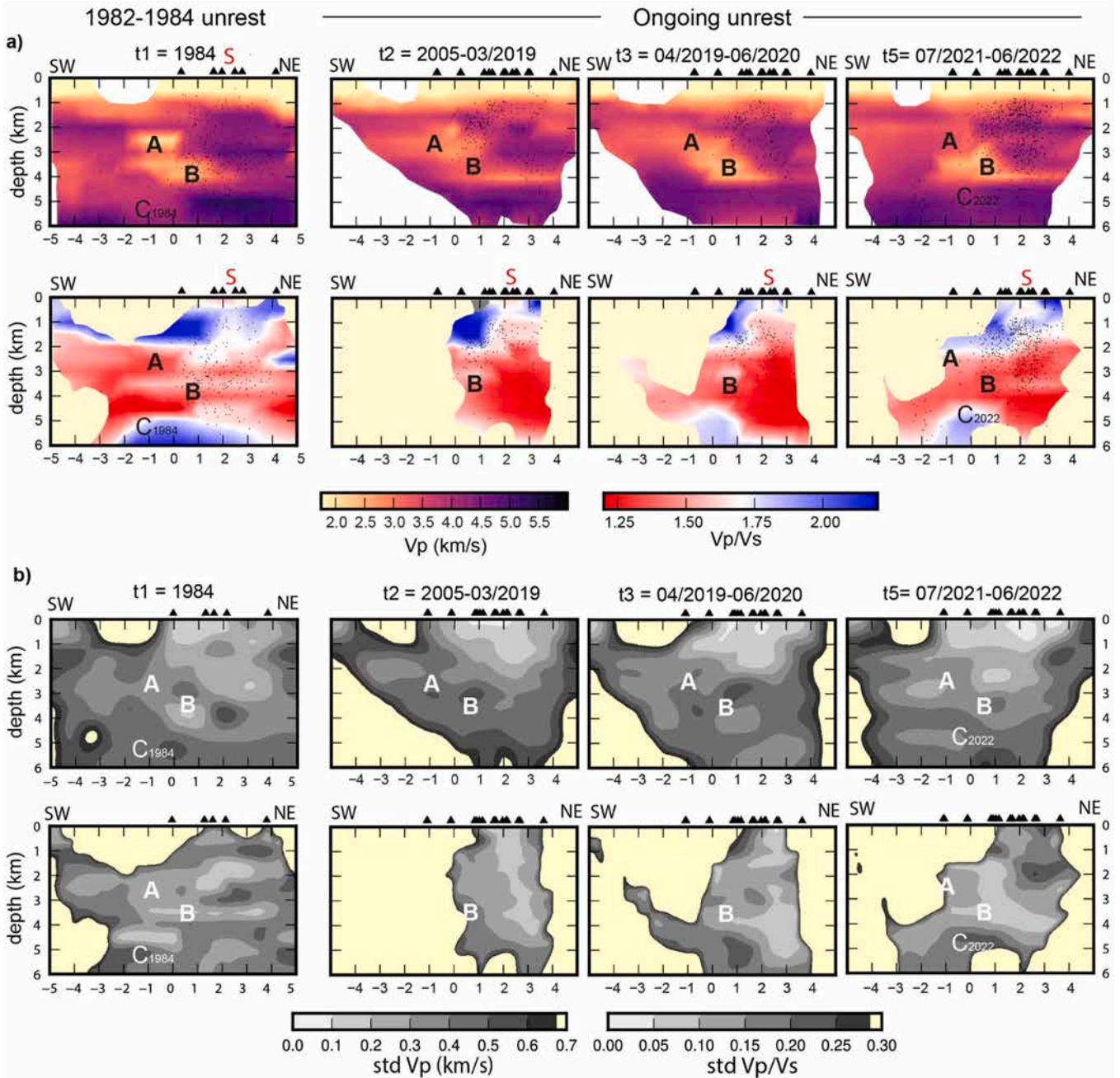**Fig. 5.** a) Time variations of the posterior mean Vp (upper panels) and Vp/Vs (lower panels) plotted on the SW-NE vertical cross-section (see Fig. 3a for the position). Uniform white and yellow areas are not-resolved model regions. Black dots: earthquakes distant less than 1.5 km from the section. Triangles: stations distant less than 2 km from the section. S: Solfatara, A-B: central reservoirs, C: deep reservoir. b) Posterior Vp standard deviations (upper panels) and posterior Vp/Vs standard deviations (lower panels) plotted on the same section.

anomaly: Vp=3.2 km/s, Vp/Vs=2.10). The A and C anomalies are included in the same test because they are distant enough to prevent trade-off between them. The results show a very good recovery of the A and B anomalies (Figs. S8-S9), in both shape and amplitude. The C anomaly is also recovered in both the Vp and Vp/Vs models (Fig. S8), although with a worse recovery of the shape.

3.2. Time dependent 4D Vp and Vp/Vs models

The time-dependent 4D Vp and Vp/Vs models reveal remarkable changes over time (Figs. 5-8): (i) the A anomaly is characterized by a remarkable Vp increase during the current unrest (t2-t5) compared to 1984 (up to 1.5 km/s, Figs. 6a,b), associated with a Vp/Vs increase (0.1–0.2). (ii) the B anomaly shows a similar Vp increase (up to 1 km/s,

Figs. 5a,6,8a), but restricted to the second period (t2=2005–03/2019), and associated with a progressive Vp/Vs decrease (up to 0.3, Figs. 6a,c).

The Vp change in the A anomaly is generally more than double if compared to the posterior error (σ_{Vp}=0.3–0.4 km/s, Fig. 5b), whereas the Vp/Vs change is comparable to posterior error ($\sigma_{Vp/Vs}$=0.15, Fig. 5b). The results of the spike test (Figs. S11, S14) revealed that the A anomaly can be well recovered in both shape and amplitude, in all time-steps, in the Vp model. In the Vp/Vs model, the anomaly is recovered with a decreased amplitude and a worse shape for all time-steps except 1984 (t1). Therefore, the Vp changes over time have to be considered reliable and not caused by the different illumination of the target volume in different periods. Conversely, the Vp/Vs changes can be considered with more caution.

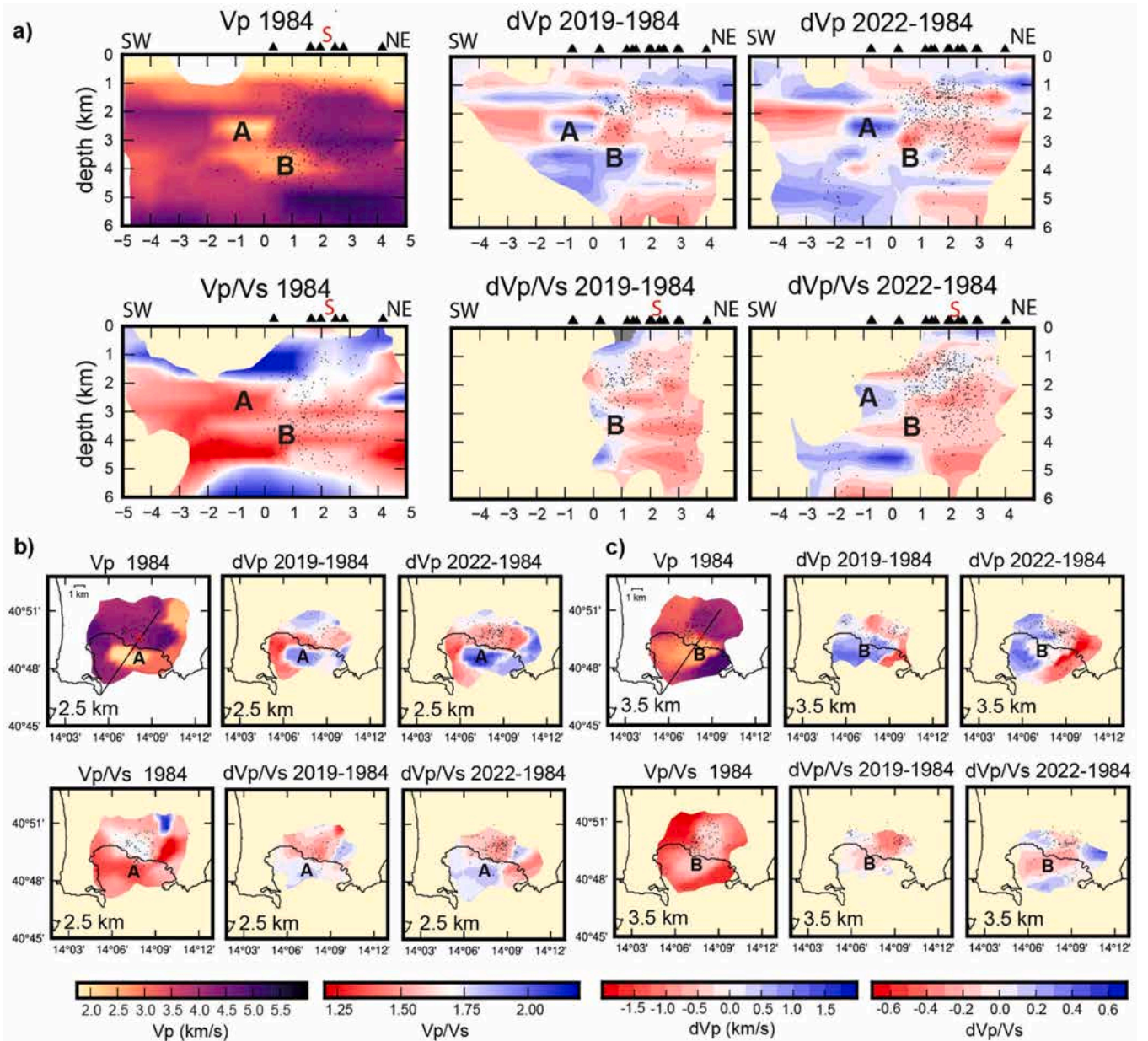The Vp change in the B anomaly is also generally more than double if

Fig. 6. Velocity changes into the central reservoirs A e B. a) Vp model (upper, left panel) and Vp/Vs model (lower, left panel) in 1984 time-step (t1) and absolute Vp and Vp/Vs differences between 2019 and 1984 (t2-t1, central panels) and 2022 (t5-t1, right panels). Uniform white and yellow areas are not-resolved model regions. Black dots: earthquakes distant less than 1.5 km from the section. Triangles: stations distant less than 2 km from the section. S: Solfatara, A-B: central reservoirs. b-c) Vp and Vp/Vs models in 1984 (left panels) and absolute Vp and Vp/Vs differences between 2019 and 1984 (t2-t1, central panels) and 2022 (t5-t1, right panels), plotted on layers at 2.5 (b) and 3.5 km (c) depth. Uniform white and yellow areas are not-resolved model regions. A-B: central reservoirs. Posterior standard deviations of the layers are provided in the supplementary Fig. S16.

compared to the posterior error (σ_{Vp}=0.2–0.6 km/s, Fig. 5b), whereas the Vp/Vs change is higher than posterior error ($\sigma_{Vp/Vs}$=0.1–0.2, Fig. 5b). The results of the spike test (Figs. S12, S15) revealed that the B anomaly can be similarly resolved in all time-steps except the t2 time-step (2005–03/2019), in both the Vp and Vp/Vs models. Moreover, the absolute differences between the amplitudes recovered in 2005–03/2019 (t2) and 1984 (t1) amounts to 0.5 km/s and 0.2 for Vp and Vp/Vs, respectively. Therefore, the strong reduction in the B anomaly observed after 1984 (t1) can be considered reliable, as well as the general trend of decreasing Vp/Vs over time.

At shallow depth the 4D velocity model revealed two interesting features not observed in the 3D model: (i) a progressive Vp and Vp/Vs decrease below the Solfatara emission zone, between 1984 and 2020 (t3) (Fig. 5a, depth 1–2.5 km, dVp~1 km/s, dVpVs~0.2) and (ii) the existence of a high Vp layer, located at 1.5–2 km depth, that becomes more evident and continuous over time (Fig. 7a). In both the cases, the overall posterior σ (Figs. 5b and 7b) are remarkably lower than in the 3D model (Fig. 4b), suggesting that time-dependent velocity models are able to fit the data much better than the static 3D model. The low values of posterior σ, if compared to the amplitude of velocity changes, strongly support the reliability of the observed velocity changes over time.

The C anomaly (Figs. 5a and 8) is well visible in 1984 (t1) and reappears only after 04/2019 (t3), with a narrower shape, decreased amplitude and shifted position. Moreover, since 04/2019 (t3), it seems to be shallower than in 1984, with a strong Vp/Vs increase in between 4.5 and 5 km depth (>0.4, Fig. 8).
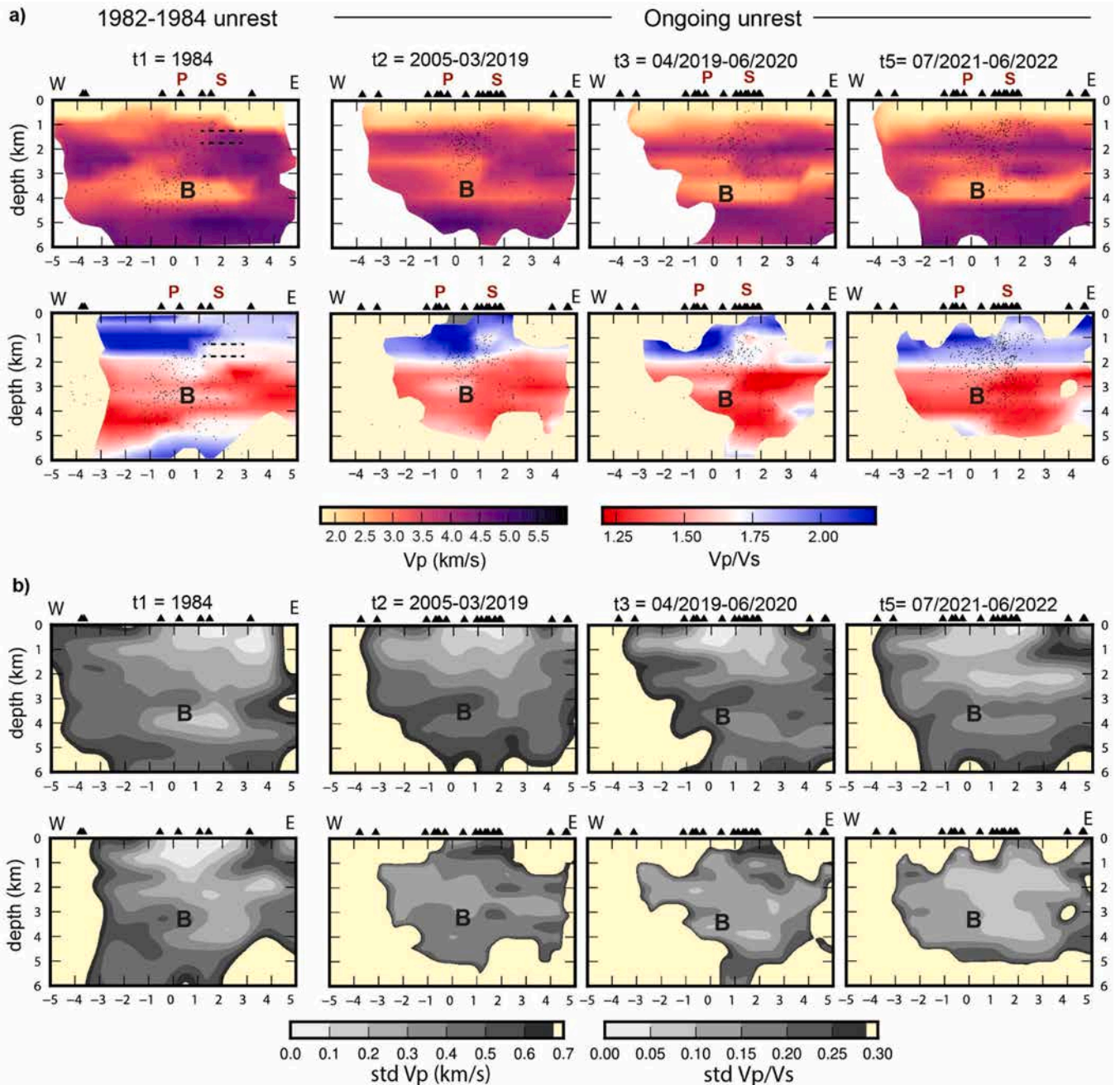

Fig. 7. a) Time variations of the posterior mean Vp (upper panels) and Vp/Vs (lower panels) plotted on the W-E vertical cross-section (see Fig. 3a for the position). Uniform white and yellow areas are not-resolved model regions. Black dots: earthquakes distant less than 1.5 km from the section. Triangles: stations distant less than 2 km from the section. S: Solfatara, P:Pozzuoli town. B: central reservoir. b) Posterior Vp standard deviations (upper panels) and posterior Vp/Vs standard deviations (lower panels) plotted on the same section.
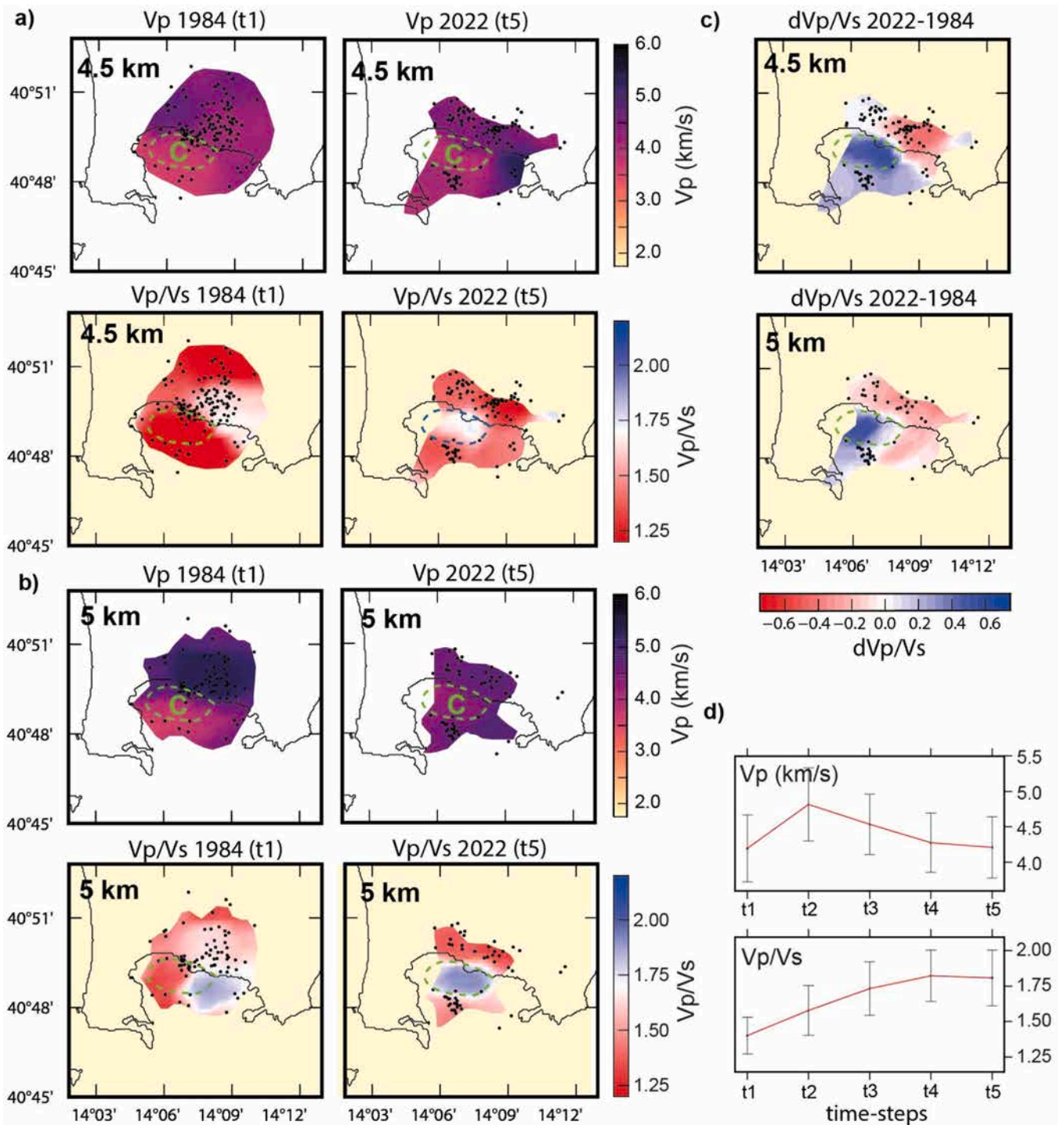
Fig. 8. Velocity changes into the deep reservoir C. a) Vp and Vp/Vs models in 1984 (left panels) and 2022 (right panels) plotted on the horizontal layer at 4.5 km depth. Green dashed curves mark model regions where Vp and Vp/Vs values may indicate the accumulation of magma during the current unrest. Uniform white and yellow areas are not-resolved model regions. b) Vp and Vp/Vs models in 1984 (left panels) and 2022 (right panels) plotted at 5 km depth. c) Vp/Vs differences between 2022 (t5) and 1984 (t1) plotted at 4.5 km depth. d) Time evolution of the average Vp (upper panel) and Vp/Vs (lower panel) into the reservoir C in between 4.5 and 5 km depth (computed as average velocity of up to ten resolved grid-nodes for each time grid).

The spike test (Figs. S13-S14) revealed that the amplitude of the C anomaly is recovered by more than 50 % in 1984 (t1) and 2021–2022 (t4-t5), in both the Vp and Vp/Vs models, and that its shape is smeared in the E-W direction. The differences between the recovered amplitude in 1984 (t1) and 2022 (t5) are lower than 0.5 km/s and 0.2, for Vp and Vp/Vs, respectively. Between 2005 and 2020 (t2-t3) the resolution is questionable, because the Vp and Vp/Vs are only partially and locally recovered.

Since different time-steps show different resolving capability in between 4.5 and 5 km depth, we computed the average Vp and Vp/Vs values into the volume characterized in 2022 (t5) by low Vp, high Vp/Vs (Vp<4.25 km/s, Vp/Vs>1.7) and absence of seismicity (Fig. 8, dashed line). The same computation was performed, for each time-step, by considering only the resolved grid-nodes (i.e. nodes with the posterior σ lower than the prior one). The results highlight the general trends over

time of Vp and Vp/Vs (Fig. 8d): (i) a notable Vp increase (up to 0.75 km/s) from 1984 (t1) to 2019 (t2), followed by a decrease in later periods. (ii) a remarkable Vp/Vs increase, from 1.4 to 1.8, between 1984 (t1) and 2022 (t5). These velocity changes are higher than both the posterior σ and the different recovery capability highlighted by the spike test. Therefore, we can conclude that the general trend of velocity changes over time into the C anomaly is reliable, as well as the differences between the values found in 2022 compared to 1984.

Another strong Vp reduction (<4 km/s, Fig. 5a) is also visible at 6 km depth in 2019–2020 (t2-t3), but resolution tests show conflicting results about the reliability of the velocity model at this depth, depending on the size of the anomaly, and further data are needed to support it.

4. Discussion

4.1. Shallow structure (0–2 km): buried caldera rim and Solfatara emission zone

The high Vp (> 4 km/s) annular anomaly observed at 1–1.5 km depth corresponds to the buried rim of the caldera (Fig. 3), formed after the Neapolitan Yellow Tuff eruption, and consisting of high density hydrothermalized volcanic formations (De Lorenzo et al., 2001; Zollo et al., 2003; Judenherc and Zollo, 2004). The low Vp (< 2.5 km/s) and high Vp/Vs (> 2.1) volume, with maximum values found beneath the town Pozzuoli, is consistent with the presence of water-saturated, highly-fractured rocks, related to the post-caldera activity, as also inferred from seismic attenuation (De Lorenzo et al., 2001; Calò and Tramelli, 2018) and scattering studies (Tramelli et al., 2006). The Vp/Vs strong decrease at depth of about 2 km is expected, due to the occurrence of the liquid-gas state transition inferred at this depth for the Campi Flegrei area (Caliro et al., 2007; Arienzo et al., 2010). In the case of porous media with liquid content, the Vp/Vs ratio is in fact usually high, whereas it may significantly lower in the presence of gas or hot-water with sufficient water steam (Takei, 2002; Koulakov et al., 2013; Ivanov et al., 2016). All these features are consistent with previous tomographic studies (Vanorio et al., 2005; Chiarabba and Moretti, 2006; Battaglia et al., 2008; De Siena et al., 2010; Priolo et al., 2012; Calò and Tramelli, 2018).

At shallow depth, the time-dependent 4D model reveals a remarkable decrease in Vp/Vs (Fig. 5a), in between 1 and 2 km depth, below the Solfatara emission zone. The decrease is evident from 1984 until 2020. The lowering Vp/Vs may reflect a shallowing liquid-gas transition, due to increasing temperatures. This interpretation is consistent with the contemporary increase in temperature and pressure inferred from the CO concentration measured at Solfatara fumaroles (Caliro et al., 2007; INGV). Moreover, the main shallowest seismicity occurs inside the low Vp/Vs volume. This evidence confirms this area as a preferential pathway for the ascent of hot fluids triggering seismicity, due to energy transfer from hot fluids to hosting rocks (Chiodini et al., 2021).

4.2. Plumbing system: central reservoirs

The existence of a low Vp anomaly beneath the caldera is not a novelty (Vanorio et al., 2005; Chiarabba and Moretti, 2006; Battaglia et al., 2008; De Siena et al., 2010; Priolo et al., 2012; Calò and Tramelli, 2018). Nevertheless, thanks to the use of a self-adaptive parameterization, its internal structure is defined by our 3D model with higher details, showing two main "sill-like" structures (A and B anomalies in Figs. 3 and 4). The low Vp anomalies are characterized by sparse seismicity, while most of the earthquakes occur within the higher Vp surrounding rocks to the east.

The detection of potential magma and/or gas reservoirs from Vp and Vp/Vs is not straightforward. The most suggestive parameter is the Vp/Vs ratio, because it is particularly sensitive to porosity and the presence of fluids and melts (Takei, 2002; Koulakov et al., 2013; Ivanov et al., 2016). The generally low Vp/Vs values (1.4–1.75) of the reservoirs

argue against the presence of relevant amounts of melt. They can be more likely related to the accumulation of magmatic fluids into gas-bearing, fractured and overpressured formations at supercritical condition, as already inferred and modeled by Vanorio et al. (2005). Nevertheless, the presence of melt in the reservoir volumes with the higher Vp/Vs values (up to 1.75) cannot be ruled out.

Anyway, regardless of composition, the low Vp anomaly fits well the source of inflation/deflation inferred from gravity and deformation data (Amoruso et al., 2008; Amoruso and Crescentini, 2022) and attenuation data (De Siena et al., 2017a), corroborating the idea that this is the main volume of storage for magmatic fluids, cyclically fed from the underlining magma reservoir and which in turn supplies the overlaying hydrothermal system.

The increase in both the Vp and Vp/Vs observed in the shallower reservoir A between 1984 and 2019 (Figs. 5 and 6) may be consistent with a process of cooling and degassing, probably started after 1984. Both the decrease in temperature and the reduced overpressure are processes able to increase the Vp and Vp/Vs ratio. Conversely, the decrease in both Vp and Vp/Vs observed into the reservoir B suggests a process of recharge and re-pressurization by magmatic fluids, occurred during the current unrest.

A final remarks regards the existence of a thin, high strength, low permeability layer at 1.5–2 km depth in the caprock formations, which was previously inferred based on seismic tomography (Calò and Tramelli, 2018), attenuation studies (Akande et al., 2019), and the peculiar mechanical properties measured on Tuffite samples from the Agip wells (Vanorio and Kanitpanyacharoen, 2015). High Vp and low Vp/Vs are expected because of the higher values of elastic moduli, especially the shear modulus (Vanorio and Kanitpanyacharoen, 2015). In the 4D model (Fig. 7), the existence of a thin high velocity layer above the central reservoirs is much more evident during the current unrest compared to the 1982–1984 one. We hypothesize that the appearance of a thin caprock layer above the central reservoir could be related to self-sealing processes that have occurred after 1984. It is noteworthy that the data used to compute the 1984 model refer only to the end of the 1982–1984 unrest episode, when the caprock layer likely broke, promoting depressurization processes that favored the occurrence of subsidence (Lima et al., 2021; Danesi et al., 2024).

Finally, the average Vp and Vp/Vs decrease observed between 1984 and 2022 in the volume where the most seismicity occurred (Fig. 6a), suggests that prolonged unrest have favored an increase of fracturing and cracks opening (Dvorkin and Nur, 1996), likely due to the increased pore pressure by gas released from depth.

4.3. Plumbing system: deep reservoir

The main new findings of our tomographic model compared to the previous ones is the remarkable low Vp and high Vp/Vs anomaly imaged at 5 km depth below the central part of caldera (C anomaly, Figs. 3 and 4). This volume is clearly aseismic and is surrounded by deeper seismicity, mainly located in the higher Vp, lower Vp/Vs surrounding rocks. Although the Vp decreases and the Vp/Vs increases at increasing temperature, the effect is considered much less relevant than the fluid content (Christensen, 1996). Thus, the observed Vp and Vp/Vs values suggest the existence of a magma storage zone (see also Section 4.4). The inferred depth is consistent with the depth suggested by thermal profiles extrapolated from well data for the past activity of Campi Flegrei (Lima et al., 2021). It is also in agreement with the magmatic source inferred from historical, archeological, and geological record of Campi Flegrei caldera (Di Vito et al., 2016) and from gravity and deformation data (Gottsmann et al., 2006; Amoruso et al., 2014). The inferred magmatic body is separated from the overlaying low Vp anomalies by a thin high Vp layer, which may be interpreted as the crystallized layer confining magma at depth. The loss of resolution at depth greater than 6 km prevents us from defining the connection with deeper sills (Zollo et al., 2008; Costanzo and Nunziata, 2017; Fedi et al., 2018).

This deep reservoir shows remarkable velocity changes over time (Figs. 5 and 8). It is well visible in 1984, with Vp and Vp/Vs values consistent with the presence of magma (see Section 4.4). A similar anomaly, albeit reduced and shifted, progressively reappears after 04/2019, reaching shallower depth (4.5 km). At this depth, the increase in Vp/Vs between 1984 (Vp/Vs=1.4) and 2022 (Vp/Vs=1.8) is remarkable. Moreover, the very low Vp/Vs ratio found in 1984 is not consistent with the presence of melt (see Section 4.4). This suggests that a small batch of magma has accumulated during the current unrest. The occurrence of a magmatic recharge starting in 2019 could also be linked to the progressive deepening of crustal seismicity in the volume around the reservoir, and the notable step in seismic energy release observed at the end of 2019 (Fig. 1).

4.4. Melt fraction computation

To further test the hypothesis that the deep low Vp and high Vp/Vs volume is compatible with the presence of magma, we compared the Vp and Vp/Vs values with theoretical values obtained by considering a crystal mush with fluid-saturated pore space (Chu et al., 2010; Paulatto et al., 2022) and different porosity values. We hypothesized a magmatic reservoir formed by hosting rocks of syenitic composition (D'Antonio, 2011), saturated with hydrous trachytic melts (Misiti et al., 2011; wt 0–8 %), which are the dominant erupted magmas during the whole volcanic history of the caldera (Buono et al., 2022). Theoretical Vp and Vp/Vs of the assemblage were calculated with Gassmann's relations (Gassmann, 1951; see Chu et al. 2010 for detail about the mathematical formulation and Table S3 for calculation parameters). The comparison between theoretical and observed velocities (Fig. 9) indicates that the velocity values found within the C reservoir in the 3D model, in 1984 and 2022 are compatible with the presence of magma. Conversely, the low Vp/Vs ratio observed in 1984 at 4.5 km depth is not compatible. If we consider the magmatic reservoir as the volume with lower Vp and higher Vp/Vs compared to the surrounding zone and lack of seismicity, we can obtain a rough estimation of magma volumes. The melt-fractions would amount to 24 % in the 3D model, 21 % in 1984, and 17 % in 2022. The approximate reservoir volume estimated in 2022 (marked by the dashed curve in Fig. 8) is 1.3km^3, with a magma volume of 0.2km^3.

It is noteworthy that the Gaussman's relations are valid only under the assumptions that pore pressure is in equilibrium between pores and the pores are in flow communication, therefore neglecting any overpressures. Despite the choice of different values of P and T revealed a limited pressure-temperature dependence of material properties on this calculation, suggesting that neglecting overpressures in the reservoirs should not significantly affect the results, the estimated melt fractions and magma volumes have to be considered only indicative.

5. Conclusions

We identify the overall structure of the Campi Flegrei caldera and the main residence volume of magma, with transient anomalies that trace sharp changes in the system, due to renewed magma injection and increase in temperature and steam production.

The plumbing system (Fig. 10) consists of multiple intrusions in the central part of the caldera and a main magma reservoir at about 5 km depth. Transient changes in elastic parameters reveal that the Campi Flegrei caldera is experiencing a multi-phase unrest, in which both a main deep magma reservoir and the overlaying plumbing system are being recharged. The central reservoir appears to have been recharged by magmatic fluids during the 1982–1984 unrest and, after a period of possible degassing, also during the current unrest. Despite the main magmatic infill of the deep reservoir seems to have occurred during the 1982–1984 unrest, our results reveal a new injection of magma in the deep reservoir, possibly starting in 2019, which could testify a new phase of magma accumulation and reorganization.

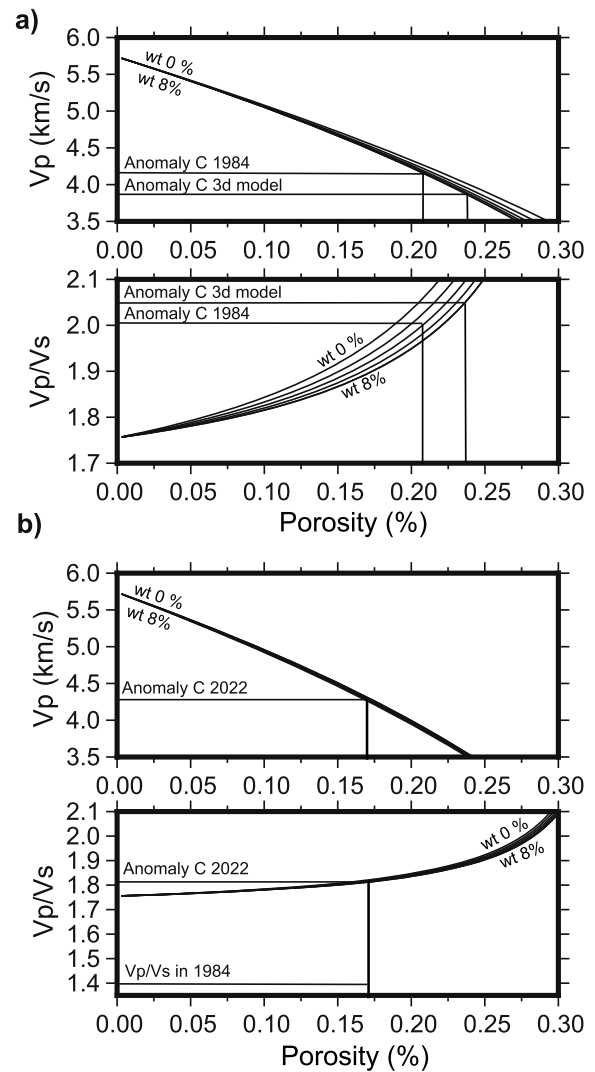The concentration of seismicity in a vertically elongated column

Fig. 9. a) Theoretical Vp and Vp/Vs in syenitic rocks filled with hydrous trachitic melt (wt % H$_2$O 0–8, steps by 2 %) and supercritical H$_2$O − CO$_2$ (1 % of porosity) as a function of porosity. Black horizontal lines indicate the average Vp and Vp/Vs observed into the reservoir C in the 3d model and in 1984. Vertical black lines indicate the porosity value that fits both the Vp and Vp/Vs. The melt fraction is equal to the best fit porosity value, because pores are considered fluid-filled. b) Same computation with more H$_2$O − CO$_2$ (3 % of porosity). Black horizontal lines indicate the average Vp and Vp/Vs observed into the reservoir C in 2022. The Vp/Vs observed into the reservoir in 1984 is shown for comparison.

directly below the Solfatara, together with the observed transient velocity changes, suggests an overproduction of hot fluids ascending from the deep reservoir, which trigger seismicity and cause a continuous weakening and fracturing of the crust. The repetition of such processes during continued unrest results in the long term growth of the plumbing system and favors more extensive fracturing. The episodic transfer of melts during unrest phenomena can be a common process at unresting calderas, and the eventual eruption of magma depends on how ephemeral such injections are, and on the local depressurization of the burden cover associated with the lateral migration of magma.

CRediT authorship contribution statement

G. Giacomuzzi: Writing – original draft, Software, Methodology, Investigation, Formal analysis, Data curation, Conceptualization. **C. Chiarabba:** Writing – original draft, Validation, Supervision,
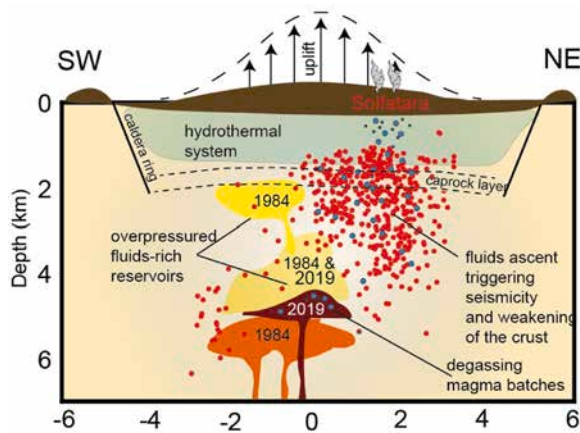
Fig. 10. Summary interpretative sketch of the caldera. Main zones of accumulation of magma (brown - orange) and magmatic fluids/magma (yellow). Years refer to the inferred time of magma/fluids injections. Red dots mark seismicity, vertical arrows indicate the ongoing uplift in the resurging zone and blue dots gas ascent.

Conceptualization. **F. Bianco:** Writing – original draft, Supervision, Conceptualization. **P. De Gori:** Validation, Supervision. **N. Piana Agostinetti:** Supervision, Methodology.

Declaration of competing interest

The authors declare that they have no known competing financial interests or personal relationships that could have appeared to influence the work reported in this paper.

Data availability

Seismic waveforms, locations and magnitudes of earthquakes used in this study are available since 2016 at http://terremoti.ov.ingv.it/gossip/flegrei. Previous catalog, without waveforms, is available at http://sismolab.ov.ingv.it/sismo/index.php PAGE=SISMO/last&area=Flegrei. Waveforms between 1984 and 2015 are available upon request at direzione.ov@ingv.it. Figures have been produced using open–source software GMT (https://www.generic-mapping-tools.org/).

The 3D and 4D velocity models and the earthquake coordinates obtained in this study are available at https://data.mendeley.com/datasets/s9xmxv9skg/1.

Acknowledgments

Supplementary materials

Supplementary material associated with this article can be found, in the online version, at doi:10.1016/j.epsl.2024.118744.

References

Acocella, V., 2019. Bridging the gap from caldera unrest to resurgence. Front. Earth Sci. 7 https://doi.org/10.3389/feart.2019.00173.

Acocella, V., Di Lorenzo, R., Newall, C., Scandone, R., 2015. An overview of recent (1988-2014) caldera unrest: knowledge and perspectives. Rev. Geophys. 53, 896–955.

Akande, W., Gan, Q., Cornwell, D., De Siena, L., 2021. Thermo-hydro-mechanical model and caprock deformation explain the onset of an ongoing seismo-volcanic unrest. J. Geophys. Res.: Solid Earth 126. https://doi.org/10.1029/2020JB020449.

Akande, W.G., De Siena, L., Gan, Q., 2019. Three-dimensional kernel-based coda attenuation imaging of caldera structures controlling the 1982-84 Campi Flegrei unrest. J. Volcanol. Geotherm. Res. 381, 273–283. https://doi.org/10.1016/j.jvolgeores.2019.06.007.

Amoruso, A., Crescentini, L., 2022. Clues of ongoing deep magma inflation at Campi Flegrei Caldera (Italy) from empirical orthogonal function. Anal. SAR Data Remote Sens 14.

Amoruso, A., Crescentini, L., Berrino, G., 2008. Simultaneous inversion of deformation and gravity changes in a horizontally layered half-space: evidences for magma intrusion during the 1982–1984 unrest at Campi Flegrei caldera (Italy). Phys. Earth Planet. Inter. 272, 181–188.

Amoruso, A., Crescentini, L., Sabbetta, I., 2014. Paired deformation sources of the campi flegrei caldera (italy) required by recent (1980–2010) deformation history. Solid Earth 119, 858–879.

Arienzo, I., Moretti, R., Civetta, L., Orsi, G., Papale, P., 2010. The feeding system of Agnano-Monte Spina eruption (Campi Flegrei, Italy): dragging the past into present activity and future scenarios. Chem. Geol. 270, 135–147.

Battaglia, J., Zollo, A., Virieux, J., Dello Iacono, D., 2008. Merging active and passive data sets in traveltime tomography: the case study of Campi Flegrei caldera (southern Italy). Geophys. Prospect. 56, 555–573.

Bodin, T., Sambridge, M., Gallagher, K., 2009. A self-parametrizing partition model approach to tomographic inverse problems. Inverse Prob. 25, 1–22.

Buono, G., Paonita, A., Pappalardo, L., Caliro, S., Tramelli, A., Chiodini, G., 2022. New insights into the recent magma dynamics under Campi Flegrei caldera (Italy) from petrological and geochemical evidence. J. Geophys. Res.: Solid Earth 127.

Caliro, S., Chiodini, G., Moretti, R., Avino, R., Granieri, D., Russo, M., Fiebig, J., 2007. The origin of the fumaroles of La Solfatara (Campi Flegrei, south Italy). Geochim. Cosmochim. Acta 71, 3040–3055.

Calò, M., Tramelli, A., 2018. Anatomy of the Campi Flegrei caldera using enhanced seismic tomography models. Sci. Rep. 8.

Chiarabba, C., De Gori, P., Boschi, E., 2009. Pore-pressure migration along a normal-fault system resolved by time-repeated seismic tomography. Geology 37, 67–70.

Chiarabba, C., De Gori, P., Segou, M., Cattaneo, M., 2020. Seismic velocity precursors to the 2016 Mw 6.5 Norcia (Italy) earthquake. Geology 48, 924–928.

Chiarabba, C., Moretti, M., 2006. An insight into the unrest phenomena at the Campi Flegrei caldera from Vp and Vp/Vs tomography. Terra Nova 18, 373–379.

Chiodini, G., Caliro, S., Avino, R., Bini, G., Giudicepietro, F., De Cesare, W., Ricciolino, P., Aiuppa, A., Cardellini, C., Petrillo, Z., Selva, J., Siniscalchi, A., Tripaldi, S., 2021. Hydrothermal pressure-temperature control on CO_2 emissions and seismicity at Campi Flegrei (Italy). J. Volcanol. Geotherm. Res. 414, 107245 https://doi.org/10.1016/j.jvolgeores.2021.107245.

Chiodini, G., Paonita, A., Aiuppa, A., Costa, A., Caliro, S., De Martino, P., Acocella, V., Vandemeulebruck, J., 2016. Magmas near the critical degassing pressure drive volcanic unrest towards a critical state. Nat. Commun. 7, 1–9.

Christensen, N., 1996. Poisson's ratio and crustal seismology. J. Geophys. Res. 101, 3139–3156.

Chu, R., Helmberger, D., Sun, D., Jackson, J., Zhu, L., 2010. Mushy magma beneath yellowstone. Geophys. Res. Lett. 37.

Costanzo, M., Nunziata, C., 2017. Inferences on the lithospheric structure of Campi Flegrei District (southern Italy) from seismic noise cross- correlation. Phys. Earth Planet. Interiors 265, 92–105.

Danesi, S., Pino, N.A., Carlino, S., Kilburn, C.R., 2024. Evolution in unrest processes at Campi Flegrei caldera as inferred from local seismicity. Earth Planet. Sci. Lett. 626, 118530 https://doi.org/10.1016/j.epsl.2023.118530.

De Lorenzo, S., Zollo, A., Mongelli, F., 2001. Source parameters and three-dimensional attenuation structure from the inversion of microearthquake pulse width data: qp imaging and inferences on the thermal state of the Campi Flegrei caldera (southern Italy). J. Geophys. Res. 106, 16287–16306. https://doi.org/10.1029/2000JB900463.

De Martino, P., Dolce, M., Brandi, G., Scarpato, G., Tammaro, U., 2021. The ground deformation history of the Neapolitan volcanic area (Campi Flegrei Caldera, Somma–Vesuvius Volcano, and Ischia Island) from 20 years of continuous GPS observations (2000–2019). Remote Sens 13.

De Siena, L., Amoruso, A., Del Pezzo, E., Wakeford, Z., Castellano, M., Crescentini, L., 2017a. Space-weighted seismic attenuation mapping of the aseismic source of Campi Flegrei 1983–1984 unrest. Geophys. Res. Lett. 44, 1740–1748. https://doi.org/10.3390/rs13142725.

De Siena, L., Chiodini, G., Vilardo, G., Del Pezzo, E., Castellano, M., Colombelli, S., Tisato, N., Ventura, G., 2017b. Source and dynamics of a volcanic caldera unrest: Campi Flegrei, 1983–84. Sci. Rep. 7, 1–13. https://doi.org/10.1038/s41598-017-08192-7. URL.

De Siena, L., Pezzo, E.D., Bianco, F., 2010. Campi Flegrei seismic attenuation image: evidences of gas reservoirs, hydrotermal basins and feeding systems. J. Geophys. Res. 115, 9312–9329.

Di Vito, M., Acocella, V., Aiello, G., Barra, D., Battaglia, M., Carandente, A., Del Gaudio, C., de Vita, S., Ricciardi, G., Ricco, C., Scandone, R., Terrasi, F., 2016. Magma transfer at Campi Flegrei caldera (Italy) before the 1538 AD eruption. Sci. Rep. 6.

Di Vito, M., Isaia, R., Orsi, A., Southon, J., de Vita, S., D'Antonio, M., Pappalardo, L., Piochi, M., 1999. Volcanism and deformation since 12,000 years at the Campi Flegrei caldera (Italy). J. Volc. Geoth. Res. 91, 221–246.

Dvorkin, J., Nur, A., 1996. Elasticity of high-porosity sandstones: theory for two North Sea datasets. Geophysics 61, 1363–1370.

D'Antonio, M., 2011. Lithology of the basement underlying the Campi Flegrei caldera: volcanological and petrological constraints. J. Volcanol. Geother. Res. 200, 91–98.

D'Auria, L., Pepe, S., Castaldo, R., Giudicepietro, G., Ricciolino, P., Tizzani, P., Casu, F., Lanari, R., Manzo, M., Martini, M., Sansosti, E., Zinno, I., 2015. Magma injection beneath the urban area of Naples: a new mechanism for the 2012–2013 volcanic unrest at Campi Flegrei caldera. Sci. Rep. 5.

Fedi, M., Cella, F., D'Antonio, M., Florio, G., Paoletti, V., Morra, V., 2018. Gravity modeling finds a large magma body in the deep crust below the Gulf of Naples, Italy. Sci. Rep. 8.

Forni, F., Degruyter, W., Bachmann, O., De Astis, G., Mollo, S., 2018. Long-term magmatic evolution reveals the beginning of a new caldera cycle at Campi Flegrei. Sci. Adv. 4.

Gassmann, F., 1951. Elastic wave through a packing of spheres. Geophysics 16, 673–685.

Giacomuzzi, G., 2013. Local Earthquake Tomography By Trans-Dimensional Monte Carlo Sampling. Studiorum—Universita' di Bologna. https://10.6092/unibo/amsdottorato/5160.

Giudicepietro, F., Chiodini, G., Avino, R., Brandi, G., Caliro, S., De Cesare, W., Galluzzo, D., Esposito, A., Rocca, A.L., Lo Bascio, D., Obrizzo, F., Pinto, S., Ricci, T., Ricciolino, P., Siniscalchi, A., Tramelli, A., Vandemeulebrouck, J., Macedonio, G., 2021. Tracking episodes of seismicity and gas transport in campi flegrei caldera through seismic, geophysical, and geochemical measurements. Seismol. Res. Lett. 92, 965–975.

Gottsmann, J., Folch, A., Rymer, H., 2006. Unrest at Campi Flegrei: a contribution to the magmatic versus hydrothermal debate from inverse and finite element modeling. J. Geophys. Res. 111.

Green, P., 2003. Trans-dimensional Markov chain Monte Carlo. High. Struct. Stoch. Syst. 27, 179–198.

INGV, . Vesuvius observatory, surveillance bulletins - https://www.ov.ingv.it/index.php/monitoraggio-e-infrastrutture/bollettini-tutti/bollett-mensili-cf/anno-2023-1.

Ivanov, A., Koulakov, I., West, M., AV, J., Gordeev, E., Senyukov, S., Chebrov, V., 2016. Magma source beneath the Bezymianny volcano and its interconnection with Klyuchevskoy inferred from local earthquake seismic tomography. J. Volcanol. Geotherm. Res. 323, 62–71.

Judenherc, S., Zollo, A., 2004. The Bay of Naples (Southern Italy): constraints on the volcanic structures inferred from a dense seismic survey. J. Geophys. Res. 33.

Koulakov, I., West, M., Izbekov, P., 2013. Fluid ascent during the 2004–2005 unrest at Mt. Spurr inferred from seismic tomography. Geophys. Res. Lett. 40, 4579–4582.

Lima, A., Bodnar, R., De Vivo, B., Spera, F., Belkin, H., 2021. Interpretation of recent unrest events (Bradyseism) at Campi Flegrei, Napoli (Italy): comparison of models based on cyclical hydrothermal events versus shallow magmatic intrusive events. Geofluids 1–16.

Malinverno, A., 2000. Bayesian criterion for simplicity in inverse problem parametrization. Geophys. J. Int. 140, 267–285.

Misiti, V., Vetere, F., Freda, C., Scarlato, P., Behrens, H., Mangiacapra, A., Dingwell, D., 2011. A general viscosity model of Campi Flegrei (Italy) melts. Chem. Geol. 290, 50–59.

Moretti, R., De Natale, G., Troise, C., 2020. Hydrothermal Versus magmatic: Geochemical Views and Clues Into the Unrest Dilemma At Campi Flegrei. Elsevier, pp. 371–406.

Mosegaard, K., Sambridge, M., 2002. Monte Carlo analysis of inverse problems. Inverse Probl. 18, R29.

Natale, J., Ferranti, L., Isaia, R., Marino, C., Sacchi, M., Spiess, V., Steinmann, L., Vitale, S., 2022. Integrated on-land-offshore stratigraphy of the Campi Flegrei caldera: new insights into the volcano-tectonic evolution in the last 15 kyr. Basin Res. 34, 855–882. https://doi.org/10.1111/bre.12643.

Newhall, C., Dzurisin, D., 1988. Historical unrest at large calderas of the world. US Geol. Surv. Bull. 1855 https://doi.org/10.3133/b1855.

Orsi, G., Di Vito, M., Isaia, R., 2004. Volcanic hazard assessment at the restless Campi Flegrei caldera. Bull. Volc. 66, 514–530.

Pappalardo, L., Buono, G., 2021. Insights Into Processes and Timescales of Magma Storage and Ascent from Textural and Geochemical Investigations. American Geophysical Union Monograph, pp. 213–235.

Pappalardo, L., Mastrolorenzo, G., 2012. Rapid differentiation in a sill-like magma reservoir: a case study from the Campi Flegrei caldera. Sci. Rep. 2.

Patanè, D., Barberi, G., Cocina, O., De Gori, P., Chiarabba, C., 2006. Time-resolved seismic tomography detects magma intrusions at Mount Etna. Science 313, 821–823.

Paulatto, M., Hooft, E., Chrapkiewicz, K., Heath, B., Toomey Douglas, D., Morgan, J., 2022. Advances in seismic imaging of magma and crystal mush. Front. Earth Sci. 10.

Piana Agostinetti, N., Giacomuzzi, G., Chiarabba, C., 2017. Seismic swarms and diffuse fracturing within Triassic evaporites fed by deep degassing along the low-angle Alto Tiberina normal fault (central Apennines, Italy). J. Geophys. Res.: Solid Earth 122, 308–331.

Piana Agostinetti, N., Giacomuzzi, G., Malinverno, A., 2015. Local 3D earthquake tomography by trans-dimensional Monte Carlo sampling. Geophys. J. Int. 201, 1598–1617.

Priolo, E., Lovisa, T., Zollo, A., Bohm, G., D'Auria, L., Gautier, S., Gentile, F., Klin, P., Latorre, D., Michelini, A., Vanorio, T., Virieuxhe, J., 2012. Campi Flegrei blind test: evaluating the imaging capability of local earthquake tomography in a volcanic area. Int. J. Geophy. 1–37.

Rosi, M., Acocella, A., Cioni, R., Bianco, F., Costa, A., De Martino, P., Giordano, G., Inguaggiato, S., 2022. Defining the Pre-Eruptive States of Active Volcanoes for Improving eruption forecasting. Front. Earth Sci 10.

Rawlinson, N., Spakman, W., 2016. On the use of sensitivity tests in seismic tomography. Geophys. J. Int. 205 (2), 1221–1243. https://doi.org/10.1093/gji/ggw084.

Sambridge, M., 1990. Menke w. 1989. geophysical data analysis: discrete inverse theory, revised edition; first edition published in 1984. San Diego, isbn 0 12 490921 3. international geophysics series volume 45. Geol. Mag. 127, 375–376. https://doi.org/10.1017/S0016756800015016.

Takei, Y., 2002. Effects of partial melting on seismic velocity and attenuation: a new insight from experiments. Annu. Rev. Earth. Pl. Sc. 45, 447–470.

Tramelli, A., Del Pezzo, E., Bianco, F., Boschi, E., 2006. 3D scattering image of the Campi Flegrei caldera (Southern Italy). Phys. Earth Planet. Interiors 155, 269–280.

Tramelli, A., Giudicepietro, F., Ricciolino, P., Chiodini, G., 2022. The seismicity of Campi Flegrei in the context of an evolving long term unrest. Sci. Rep. 12.

Trasatti, E., Magri, C., Acocella, V., Del Gaudio, C., Ricco, C., Di Vito, M., 2023. Magma transfer at Campi Flegrei caldera (Italy) after the 1538 AD eruption. Geophys. Res. Lett. 50.

Um, J., Thurber, C., 1987. A fast algorithm for two-point seismic ray tracing. Bull. Seism. Soc. Am. 77, 972–986.

Vanorio, T., Kanitpanyacharoen, W., 2015. Rock physics of fibrous rock akin to Roman concrete explains uplift at Campi Flegrei Caldera. Science 349, 617–621. https://doi.org/10.1126/science.aab1292.

Vanorio, T., Virieux, J., Capuano, P., Russo, G., 2005. Three-dimensional seismic tomography from P wave and S wave microearthquake travel times and rock physics characterization of the Campi Flegrei Caldera. J. Geophys. Res. 110 https://doi.org/10.1029/2004JB003102.

Zollo, A., Judenherc, S., Auger, E., D'Auria, L., Virieux, J., Capuano, P., Chiarabba, C., de Franco, R., Makris, J., Michelini, A., Musacchio, G., 2003. Evidence for the buried rim of Campi Flegrei caldera from 3-d active seismic imaging. Geophys. Res. Lett. 33.

Zollo, A., Maercklin, N., Vassallo, M., Dello Iacono, D., Virieux, J., Gasparini, P., 2008. Seismic reflections reveal a massive melt layer feeding Campi Flegrei caldera. Geophys. Res. Lett. 35.